




# On the Chemical Mixing Induced by Internal Gravity Waves

T. M. Rogers<sup>1,2</sup>  and J. N. McElwaine<sup>2,3</sup><sup>1</sup> School of Mathematics, Statistics and Physics, Newcastle University, Newcastle upon Tyne, UK<sup>2</sup> Planetary Science Institute, Tucson, AZ 85721, USA<sup>3</sup> Department of Earth Sciences, Durham University, Durham, UK

Received 2017 July 20; revised 2017 September 13; accepted 2017 September 13; published 2017 October 4

## Abstract

Detailed modeling of stellar evolution requires a better understanding of the (magneto)hydrodynamic processes that mix chemical elements and transport angular momentum. Understanding these processes is crucial if we are to accurately interpret observations of chemical abundance anomalies, surface rotation measurements, and asteroseismic data. Here, we use two-dimensional hydrodynamic simulations of the generation and propagation of internal gravity waves in an intermediate-mass star to measure the chemical mixing induced by these waves. We show that such mixing can generally be treated as a diffusive process. We then show that the local diffusion coefficient does not depend on the local fluid velocity, but rather on the wave amplitude. We then use these findings to provide a simple parameterization for this diffusion, which can be incorporated into stellar evolution codes and tested against observations.

*Key words:* hydrodynamics – stars: general – waves

## 1. Introduction

Accounting for hydrodynamic processes in stellar interiors over stellar evolution times has been the biggest source of uncertainty when comparing theoretical results with observations. While Mixing Length Theory (MLT) has proven extremely useful for characterizing mixing within convection zones (Bohm-Vitense 1958; Kippenhahn et al. 2012), there remain many uncertainties dealing with this mixing at convective–radiative interfaces (Renzini 1987; Zahn 1991) and within radiative regions (Pinsonneault 1997; Heger et al. 2000). Nearly all stars host radiative regions, so it is critical we develop methods for accurately parameterizing chemical mixing (and angular momentum transport) in these regions.

Numerous theoretical models have been proposed for incorporating mixing by (magneto)hydrodynamical processes in stellar radiative zones into stellar evolution models. Myriad hydrodynamic instabilities (Heger et al. 2000), rotationally induced mixing (Eddington–Sweet circulation; Eddington 1925; Vogt 1925; Sweet 1950), and magnetically induced mixing (Taylor–Spruit dynamo; Spruit 2002) have been included in modern stellar evolution codes. Still, many questions remain about mixing within stellar radiative interiors. For example, it is typically assumed that rotationally induced mixing is dominant in massive stars, yet the observed lack of correlation between nitrogen abundance and rotation rate for some stars indicates additional mixing is needed (Brott et al. 2011), and observations in multivariate parameter space suggest pulsational mixing is dominant for slow to moderately rotating OB stars (Aerts et al. 2014). Similarly, differential rotation at late stages of stellar evolution is lower than expected even when all of these mechanisms are considered (Eggenberger et al. 2017).

In general, these multi-dimensional hydrodynamic effects are parameterized as a diffusion coefficient within stellar evolution codes. Each physical process has an instability

criterion based on local properties (e.g., shear). Once instability is confirmed, a diffusion coefficient is constructed from the length scale and growth rate of the instability. This diffusion coefficient is then included locally (in space and time) in the stellar evolution calculation. While this procedure is rather rudimentary, it is clear from observations that additional mixing within stellar radiative regions is required. It is only recently, and in limited circumstances, that such prescriptions are being tested against hydrodynamic calculations that self-consistently calculate the development of the instability and the subsequent mixing induced (Edelmann et al. 2017).

Internal gravity waves (IGWs) are known to propagate and dissipate in radiative regions, which could lead to chemical mixing and angular momentum transport. However, the parameterization of IGWs in one-dimensional (1D) stellar evolution codes is complex. The transport of angular momentum by these waves cannot be treated as a diffusive process; indeed, IGWs have an *anti-diffusive* nature. That is, they drive, rather than dissipate, shear flows (Buhler 2009). For this reason, IGW transport has generally not been treated in 1D stellar evolution codes (except in the Geneva code; Charbonnel & Talon 2005; Talon & Charbonnel 2005; in which their treatment is complex). Yet, while it is clear that angular momentum transport by IGWs cannot be parameterized with a diffusion coefficient (Rogers 2015), it is unclear whether the *chemical* mixing induced by waves could be treated diffusively as previously suggested (Press & Rybicki 1981; Garcia-Lopez & Spruit 1991). The purpose of this Letter is to first determine whether wave mixing can be treated diffusively and, if so, to determine how efficient that mixing is and whether it could be reasonably parameterized in 1D stellar evolution models.

## 2. Numerics

### 2.1. Hydrodynamic Simulations

In order to measure mixing by IGWs in stellar interiors, we solve the Navier–Stokes equations in the anelastic approximation (Gough 1969; Rogers & Glatzmaier 2005). The equations are solved in two dimensions (2D) representing an equatorial slice of



Original content from this work may be used under the terms of the [Creative Commons Attribution 3.0 licence](https://creativecommons.org/licenses/by/3.0/). Any further distribution of this work must maintain attribution to the author(s) and the title of the work, journal citation and DOI.

the star. Our reference state model is that of a  $3M_{\odot}$  star with a core hydrogen content of 0.35, calculated using Modules for Experiments in Stellar Astrophysics (MESA; Paxton et al. 2010, 2015). We solve the equations from  $0.03R_*$  to  $0.70R_*$ , the initial rotation rate is uniform and equal to  $10^{-6} \text{ rad s}^{-1}$ . The simulation is run a total of  $4 \times 10^7 \text{ s}$ , or approximately 40 convective turnover times. The details of the equations and numerical methods used can be found in Rogers et al. (2013). Ideally, we would solve the equations in 3D as in Alvan et al. (2015), but few simulations such as these have been done for massive stars (Browning et al. 2004; Augustson et al. 2016) and none that include extended radiative zones. We discuss the role this reduced dimensionality might play in Section 5.

Like all hydrodynamic simulations our viscous and thermal diffusion coefficients are larger than is typical in real stars. Therefore, our waves are damped more than they would be in actual stellar interiors. Unlike the simulations presented in Rogers et al. (2012, 2013), these models are not “over-forced” so their rms velocities in the convection zone are similar to that expected from MLT (see Figure 3).

## 2.2. Tracer Particles and Diffusion

To determine whether mixing by IGWs behaves like diffusion, we introduce tracer particles within the simulation. We use tracer particles instead of solving a compositional advection–diffusion equation because such a method would require an explicit diffusion that would dominate any mixing coefficient. For simplicity we regard time as continuous and only measure radial diffusion. At some time of interest we introduce  $N$  particles, distributed uniformly in space, and track them for a time  $T$  to produce  $N$  particle trajectories (particle positions in time,  $R_i(t)$ ). We then consider all the sub-trajectories of duration  $\tau$  and use a cubic spline function  $w$  to interpolate between the start of each sub-trajectory ( $R_i(t)$ ) and the grid position. The length of a sub-trajectory (displacement of a particle) is then  $R_i(t + \tau) - R_i(t)$ . We then calculate the following profiles:

$$n(r, \tau) = \int_0^{T-\tau} \sum_{i=1}^N w(R_i(t) - r) dt, \quad (1)$$

$$P(r, \tau) = \int_0^{T-\tau} \sum_{i=1}^N w(R_i(t) - r)[R_i(t + \tau) - R_i(t)] dt, \quad (2)$$

$$Q(r, \tau) = \int_0^{T-\tau} \sum_{i=1}^N w(R_i(t) - r)[R_i(t + \tau) - R_i(t)]^2 dt. \quad (3)$$

Here,  $n(r, \tau)$  is the number of sub-trajectories starting at  $r$  of duration  $\tau$ .  $P(r, \tau)$  is the sum of the lengths of these sub-trajectories, and  $Q(r, \tau)$  is the sum of the lengths squared of these sub-trajectories. If there is a mean velocity field  $u(r)$ , then

$$u(r, \tau) = \frac{P(r, \tau)}{n(r, \tau)\tau}. \quad (4)$$

Lower values of  $\tau$  can result from many time differences, while larger values of  $\tau$  can only result for long timeline data.<sup>4</sup>

<sup>4</sup> As an example, if the time step is 1 and  $T = 100$ , a time difference of  $\tau = 10$  can result from 10–0, 11–1, 12–2, and so on, while a  $\tau$  of 98 can only result from 98–0, 99–1, and 100–2.

Therefore, low values of  $\tau$  represent more data for a given  $T$ , while larger values represent fewer data points. If particle motion is purely diffusive with zero mean, then, provided that the distance moved by particles in time  $\tau$  is smaller than the distance over which the diffusion coefficient varies, we would have

$$D(r, \tau) = \frac{Q(r, \tau)}{2n(r, \tau)\tau}, \quad (5)$$

where  $D(r, \tau)$  is the diffusion coefficient at  $r$ . If there is a mean velocity field in addition to diffusion, then we would have

$$D(r, \tau) = \frac{Q(r, \tau)}{2\tau n(r, \tau)} - \frac{P(r, \tau)^2}{2\tau n(r, \tau)^2}. \quad (6)$$

If the motion is purely diffusive, then  $D$  will not depend on  $\tau$ , but if there is a more complicated background velocity field, the situation is more complicated, as shown in the next section.

## 2.3. Wave Motion with Diffusion

In order to understand the motion of a particle in a wave acted on by diffusion, we consider a particle moving in a wave field with velocity given by  $\omega A \cos(\phi + \omega t)$  and with random fluctuations given by  $N(t)$  so that its equation of motion is

$$\frac{dx}{dt} = \omega A \cos(\phi + \omega t) + N(t). \quad (7)$$

This can be integrated to give

$$x(t) = A \sin(\phi + \omega t) + \int_0^t N(s) ds. \quad (8)$$

Now we assume that  $N(t)$  is Gaussian white noise with standard deviation  $\sigma$  so that  $\int_0^t N(s) ds = \sigma W(t)$ , where  $W(t)$  is a Wiener process (Doob 1953). We consider an ensemble of trajectories and average uniformly over the phases  $\phi$  and the Wiener process using  $\langle W(t) \rangle = 0$  and  $\langle W(t)W(s) \rangle = \min(s, t)$ . Then, we have the expectation (denoted with  $\langle \dots \rangle$ ) of the position

$$\langle x(t) \rangle = 0 \quad (9)$$

and

$$\langle [x(t + \tau) - x(t)]^2 \rangle = A^2[1 - \cos(\omega\tau)] + \sigma^2\tau. \quad (10)$$

This function of  $\tau$  is the sum of a linear function ( $A^2 + \sigma^2\tau$ ) and an oscillatory function ( $-A^2 \cos(\omega\tau)$ ). At large times ( $\tau\omega \gg 1$ ) there is a linear trend with gradient  $\sigma^2$ . From this gradient we can then extract the effective diffusion coefficient  $D = \sigma^2/2$ .

## 2.4. Application to Numerical Simulations

We carry out this procedure in post-processing. That is, given saved velocity data from our hydrodynamic simulations at time intervals  $t$ , we introduce  $N$  particles into our numerical simulation and measure  $D$  using the above procedure. Since the procedure is done in post-processing, we can include an arbitrary number of particles to check numerical convergence, and we can also vary the type of particle interpolation and the number of time steps over which we track the particles.

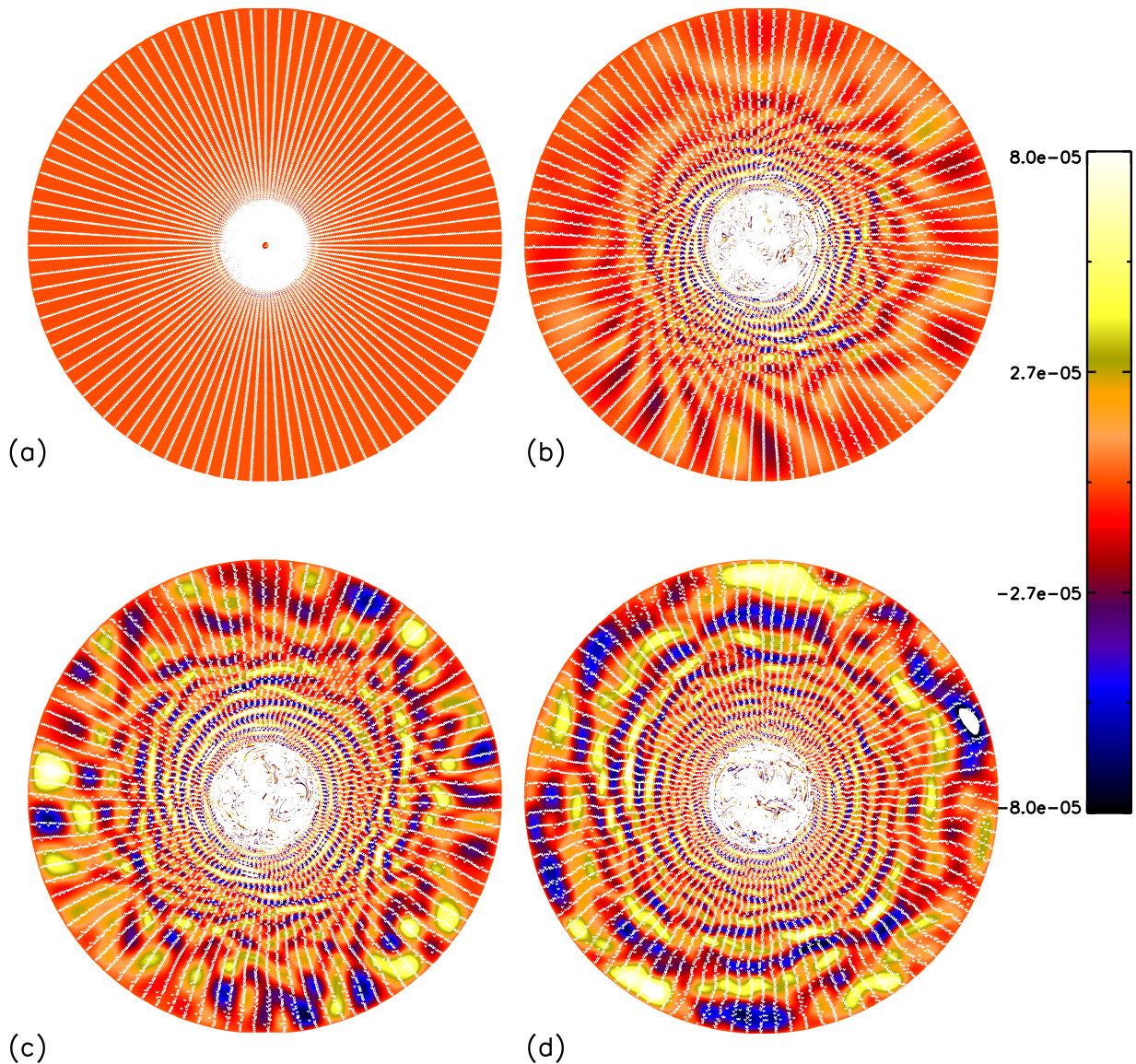


**Figure 1.** Time snapshots of vorticity (color, units are  $\text{rad s}^{-1}$ ) with particle positions, indicated with white dots overlotted. Particle positions in (a) represent a subset of the initialized particles. One can clearly see movement of the particles, in response to wave motion, in the radiation zone in (b)–(d) and particles within the convection zone are fully mixed (difficult to discern as they cover the region).

Figure 1 shows time snapshots of the vorticity and particle positions (only 15,000 shown) at four different times.

We checked our procedure against a hydrodynamic simulation with particles run within the simulation in order to confirm our velocity data was taken at fine enough time resolution. We find that in order to measure a diffusion coefficient within the radiation zone, we need long timeline data, but not very finely spaced. However, to smoothly resolve the convective–radiative interface, we need finely spaced time data over a shorter timeline. In this Letter, we are concerned with the diffusion profile within the radiation zone, so we integrate over long timelines with longer time steps and note that our convective and overshoot profile is neither well resolved nor well described as a diffusive process.

### 3. Particle Trajectories and Diffusion

The first question to address is whether the movement of particles due to the action of waves can be treated as a diffusive

process. To test this, we plot the mean squared displacement as a function of  $\tau$  in Figure 2(a) with different line types of the same color showing dependencies on the number of particles used and different colors showing different radii (see the caption for details). There, we see that at low  $\tau$  the particles indeed behave like diffusion (the mean squared displacement is a linear function of  $\tau$ ). However, at larger  $\tau$ , there is not enough data to confirm the diffusive nature. We also see that different radial levels have different slopes.

Using low values of  $\tau$  ( $2.5 \times 10^6$  s, for which we have sufficient data), we compute the diffusion coefficient as a function of radius, which is shown in Figure 2(b), again with different line types showing different numbers of particles. The vertical black solid line shows the convective–radiative interface, while the vertical black, blue, and red dashed lines show the radial positions shown in (a). There, we see that the overall radial profile of diffusion coefficient within the radiation zone is robust to variations in particle number, thus demonstrating convergence. We also see that there is a rapid transition from



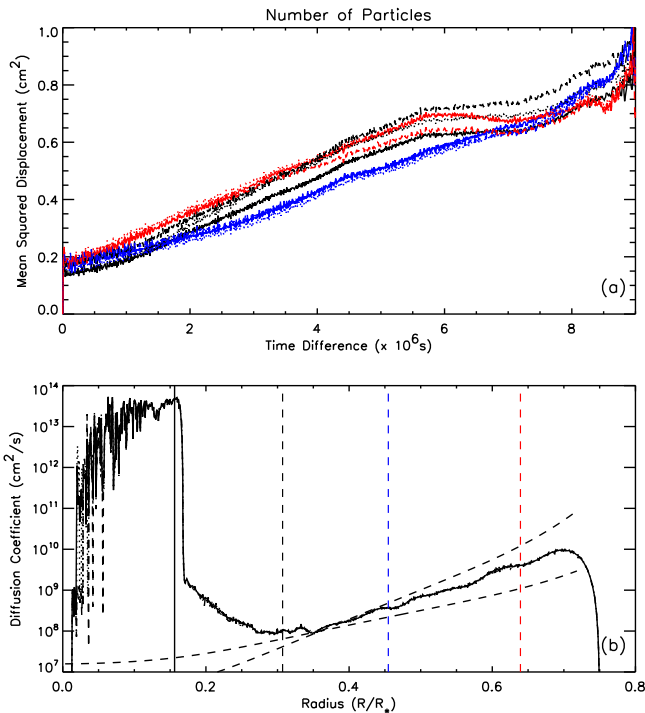


**Figure 2.** Particle diffusion. (a) Mean squared displacement as a function of time difference  $\tau$ , with total time tracked,  $T = 10^7$  s. Different colors indicate different radii (as indicated by the vertical dashed lines of the same color in (b)). (a) Different line types represent different numbers of particles with 1 million (solid line), 100,000 (dashed line), and 50,000 particles (dotted line). (b) The diffusion coefficient as a function of radius with different line types as in (a). There is no perceptible difference in diffusion coefficient within the radiative zone for varying particle number, indicating convergence. Dashed black lines represent  $\rho^{-1/2}$  and  $\rho^{-1}$ .

the behavior in the convection zone to that in the radiative region. We note that, while there is a diffusion coefficient (plotted and measured) within the convection zone and overshoot region, the behavior in those regions is generally *not* diffusive, particularly in the convection zone. The mean squared displacement as a function of  $\tau$  does not lie on a straight line. Therefore, applying a diffusion coefficient in these regions is not appropriate. However, we can see from Figure 1 that particles mix much more rapidly within the convection zone than in the radiative region, as expected.

In general, within the radiation zone, the amplitude of the diffusion coefficient rises with increasing distance from the convection zone. There is decay just outside the convection zone due to the fact that our thermal diffusivity is constant, rather than a function of radius (we discuss this in Section 4). The radial increase is proportional to a factor between  $\rho^{-1}$  and  $\rho^{-1/2}$ , which we show as black dashed lines and which we also discuss in Section 4. Therefore, we conclude that (1) IGWs mixing in the radiation zone can be treated as a diffusive process and (2) the radial profile of diffusion is robust and is proportional to a function between  $\rho^{-1}$  and  $\rho^{-1/2}$ .

#### 4. Parameterization of the Diffusion Profile

In order to find a useful parameterization of IGWs to be used in one-dimensional (1D) stellar evolution models, we would like to know both the amplitude and the radial profile of diffusion from our simulations. We find that the amplitude of the diffusion coefficient we obtain within the radiation zone is

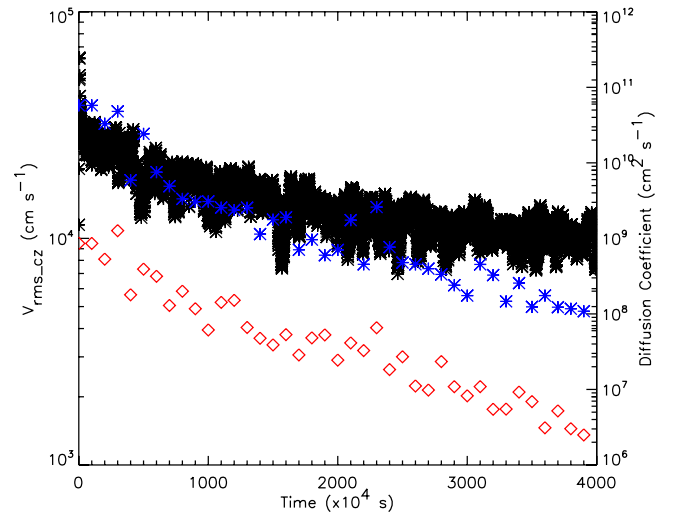


**Figure 3.** rms velocity (black asterisks) and diffusion coefficients vs. time. Diffusion coefficients are at  $0.375 R_*$  (red diamonds) and at  $0.675 R_*$  (blue asterisks) and are calculated using Equation (6) and a particle tracking time,  $T = 10^6$  s.

correlated with the rms velocity *within the convective zone*. In the model presented, the rms velocity in the convection zone is decreasing in time. This is an artifact of the fact that we force the convection through a superadiabaticity, which is reduced due to efficient convection. In previous simulations, we have used a forcing term to drive convection in order to avoid this, but here we allowed this to investigate the role of convective velocities. We see how this decay affects the diffusion coefficient in the radiation zone in Figure 3—as convective velocities decrease, the diffusion coefficient decreases. As we show later, this is because the rms velocity within the convection zone sets the wave amplitudes within the radiation zone. Within a 1D stellar evolution code, the rms velocity could be approximated as the convective velocity given by MLT.

Independent of the amplitude of the diffusion coefficient, we find that the radial profile of diffusion seen in Figure 2 is robust across choices of numerical diffusion (the thermal and viscous diffusivity are each varied by an order of magnitude) and convective velocities. Now we would like to determine what sets the radial profile of diffusion. In Figure 4, we plot the rms velocity (black asterisks), the wave amplitude squared (red crosses), and the diffusion coefficient (blue crosses) as a function of radius. The wave amplitude is calculated with Equation (12) using the largest-scale waves and all frequencies we calculate (up to  $500 \mu\text{Hz}$ ). In general, frequencies above  $\sim 40 \mu\text{Hz}$  do not contribute as their generation amplitudes are too low. We see that the diffusion profile closely correlates with the wave amplitude squared. This numerical finding is consistent with the theoretical prediction that diffusion is the autocorrelation of the Lagrangian velocity field. In this case, the velocity field is the wave amplitude, which is correlated over long timescales. The diffusion profile is *not* correlated with the local rms velocity, which is again consistent with the theoretical expectation that diffusion is the autocorrelation of the velocity field, as the local rms velocities are not correlated over long timescales and hence have negligible autocorrelation.

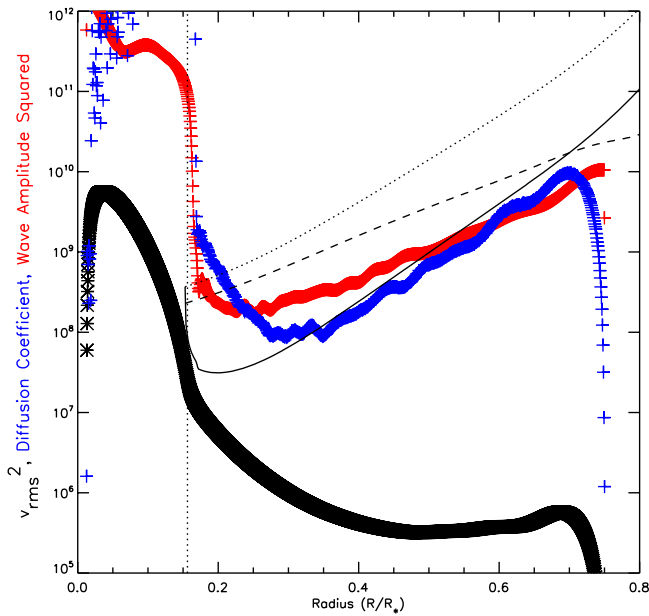


**Figure 4.** rms velocity (black asterisks;  $\text{cm}^2 \text{s}^{-2}$ ), wave amplitude squared (red crosses  $\text{cm}^2 \text{s}^{-2}$ ), and diffusion coefficient (blue crosses;  $\text{cm}^2 \text{s}^{-1}$ ) vs. radius. Wave amplitude squared is calculated using the largest-scale wave ( $k_h = 1$ ) and all frequencies. Black lines represent the wave amplitude squared calculated using Equation (12). The solid line assumes  $\kappa = 2 \times 10^{12} \text{ cm}^2 \text{ s}^{-1}$  as in the numerical simulation and a frequency spectrum at generation of velocities  $\propto \omega^{-1}$ , while the dotted and dashed lines use  $\kappa$  from MESA and a frequency spectrum at generation of velocities  $\propto \omega^{-1}$ ,  $\omega^{-3}$ , respectively.

Due to numerical constraints (dimensionality, diffusion coefficients) it is likely the IGW amplitudes in our simulations are not realistic. Using our numerical result that diffusion is proportional to the wave amplitude squared, we now turn to theoretical models for a parameterization of wave diffusion in stellar interiors. The amplitude of an IGW depends on the wave driving at the convective–radiative interface, the radiative damping of the wave, and the density stratification. The wave driving is directly correlated with the rms velocity within the convection zone,  $v_{\text{rms-cz}}$  (Garcia-Lopez & Spruit 1991). Within the radiation zone, the wave is damped by thermal diffusion (Kumar et al. 1999) and amplified by the density stratification (due to conservation of pseudomomentum; Buhler 2009). Therefore, the wave amplitude is determined from the simple function

$$v_{\text{wave}} = v_{\text{rms-cz}} \left( \frac{\rho(r)}{\rho_{\text{icz}}} \right)^{-1/2} e^{-\tau(\omega, k_h, r)}, \quad (11)$$

where  $\rho_{\text{icz}}$  is the density at the top of the convection zone. From Figure 4 we estimate the diffusion due to IGW as

$$D_{\text{mix}} = \mathcal{A} v_{\text{wave}}^2(\omega, k_h, r), \quad (12)$$

where  $\mathcal{A}$  has units of s and  $\tau(\omega, k_h, r)$  is the damping “optical depth” of a wave defined in Kumar et al. (1999) as

$$\tau(\omega, k_h, r) = \int_{r_{\text{icz}}}^r \frac{\kappa k_h^3 N^3}{\omega^4 (2\pi r)^3} dr, \quad (13)$$

where  $\kappa$  is the radiative diffusivity,  $k_h$  is the horizontal wavenumber of the wave,  $r_{\text{icz}}$  is the radius at the top of the convection zone,  $N$  is the Brunt–Väisälä frequency, and  $\omega$  is the

frequency of the wave. For simplicity, we have assumed no Doppler shift in the frequencies of the waves.  $\mathcal{A}$  is an unknown constant, which is  $\sim 1$  s in our models. Although the precise value is unknown, we do not expect it to vary significantly from this (see Section 5).

The initial decay of diffusion outside the convection zone is due to the fact that we use a constant thermal diffusion coefficient,  $\kappa$ , rather than the stellar radiative value. The numerical value used is  $2 \times 10^{12} \text{ cm}^2 \text{ s}^{-1}$  throughout, while the value in the star varies from  $10^7 \text{ cm}^2 \text{ s}^{-1}$  at the convective–radiative interface to  $10^{15} \text{ cm}^2 \text{ s}^{-1}$  at the surface of the star. Therefore, throughout our computed radiative zone, we are damping the waves more than they would be damped in the stellar interior, this is particularly true just outside the convection zone and is the reason for the initial decay seen in the wave amplitude squared (red line in Figure 4). This is demonstrated by the black lines that show the wave amplitude computed using Equation (12) with the value of  $\kappa$  used in our simulation (solid line) and the values of  $\kappa$  from the stellar model (dashed and dotted lines). For this simple calculation we have assumed that the waves are linear and non-interacting and that the wave amplitude at the convective–radiative interface is half the rms velocity.<sup>5</sup> Predictions for the frequency spectra of waves generated by convection at a given wavenumber range from  $\omega^{-3}$  (Kumar et al. 1999; Lecoanet & Quataert 2013) to  $\omega^{-1}$  (Rogers & MacGregor 2010; Rogers et al. 2013). Therefore, the dashed and dotted lines represent a frequency generation spectra of velocity proportional to  $\omega^{-3}$  and  $\omega^{-1}$ , respectively, to cover that range. We integrate over the same frequency range and scales as for the numerical results (red asterisks in Figure 4). We see that the initial decay outside the convection zone is purely an artifact of enhanced diffusion for numerical purposes and is not physical.

## 5. Discussion

In this Letter, we have demonstrated that the mixing by IGWs within radiative regions can be treated as a diffusive process. We have further shown that the local amplitude of the diffusion coefficient depends on the local wave amplitude. The wave amplitude, in turn, depends on the convective forcing ( $v_{\text{rms-cz}}$ ), the thermal damping of the wave, and the density stratification in a simple way. Therefore, a prescription for the diffusion coefficient due to mixing by IGWs can be easily implemented using Equations (11)–(13) assuming MLT velocities for the rms velocity and all other parameters determined by the stellar model. The one parameter that is left is  $\mathcal{A}$ . While this value is  $\sim 1$  s in our simulations, its precise value may depend on the stellar viscosity/thermal diffusivity, the rotation, and the dimensionality. Thermal diffusivity is already accounted for in (13). Since viscosity is enhanced in our simulations, one would expect  $\mathcal{A} = 1$  to be a lower limit. However, one does not expect viscosity to play a role in the propagation of linear waves, so the prescription in (13) where  $\mathcal{A} = 1$  likely still holds. In the case of rotation, fast rotation would likely reduce the wave amplitude, and hence  $\mathcal{A} = 1$  would be considered an upper limit, but that is likely a small effect. It is unclear what effect our reduced dimensionality has on the waves. Assuming that simple one-dimensional wave propagation is sufficient, the dimensionality likely only affects

<sup>5</sup> This amplitude comes from a simple calculation assuming  $F_w \sim MF_c$  (Lecoanet & Quataert 2013), where  $M$  is the Mach number of the convection and  $F_c$  and  $F_w$  are the convective and wave fluxes, respectively. We assume that  $F_c, F_w \sim v_c^3, v_w^3$ ; therefore,  $v_w \sim M^{1/3} v_c$ . Assuming  $M \sim 0.1$  then  $v_w \sim 0.47 v_c$ .

the wave generation spectrum. Taking all this into account, the best approach would be to assume  $\mathcal{A} = 1$  and vary the wave generation spectrum incorporated through Equation (13). Then the one parameter of the model would be the exponent of the frequency spectrum of wave generation.

Given numerical limitations, for the foreseeable future the most reliable constraints on  $\mathcal{A}$  would come from comparisons between theoretical models using this prescription and observations of slowly rotating intermediate-mass stars. Asteroseismic inversions could place constraints on near-core mixing (Moravveji et al. 2015, 2016), while spectroscopic observations may place constraints on subsurface mixing. Simultaneous comparisons between theoretical evolution models and spectroscopic and asteroseismic data could provide constraints on the entire diffusion profile and indeed may help place constraints on the wave generation spectrum.

Finally, our simulations only extend to  $0.7R_*$ . Extending our linear calculations using Equation (11) shows that the wave amplitude continues to increase until just beneath the stellar surface. It is likely that these waves break (Rogers et al. 2013), and hence the surface diffusion coefficient may be enhanced (due to turbulent mixing) beyond what is expected from linear wave behavior. Numerical simulations attempting to resolve the wave dynamics near the stellar surface will be forthcoming.

Support for this research was provided by STFC grant ST/L005549/1 and NASA grant NNX17AB92G. Computing was carried out on Pleiades at NASA Ames. T.R. thanks Conny Aerts, May Gade-Pederson, and Timothy Van Reeth for useful conversations leading to the development of this manuscript. We both thank an anonymous referee for very useful suggestions that greatly improved the manuscript.

#### ORCID iDs

T. M. Rogers  <https://orcid.org/0000-0002-2306-1362>

#### References

- Aerts, C., Molenberghs, G., Kenward, M., & Neiner, C. 2014, *ApJ*, 781, 88  
 Alvan, L., Strugarek, A., Brun, A., Mathis, S., & Garcia, R. 2015, *A&A*, 581, A112  
 Augustson, K., Brun, A., & Toomre, J. 2016, *ApJ*, 829, 92  
 Bohm-Vitense, E. 1958, *ZA*, 46, 108  
 Brott, I., Evans, C., de Koter, A., et al. 2011, *A&A*, 530, A116  
 Browning, M., Brun, A., & Toomre, J. 2004, *ApJ*, 601, 512  
 Buhler, O. 2009, Cambridge Monographs on Mechanics (Cambridge: Cambridge Univ. Press)  
 Charbonnel, C., & Talon, S. 2005, *Sci*, 309, 2189  
 Doob, J. 1953, Stochastic Processes (New York: Wiley)  
 Eddington, A. 1925, *Obs*, 48, 73  
 Edelmann, P., Röpkke, F., Hirschi, R., Cyril, G., & Jones, S. 2017, *A&A*, 604, A25  
 Eggenberger, P., Lagarde, N., Miglio, A., et al. 2017, *A&A*, 599, A18  
 Garcia-Lopez, R., & Spruit, H. 1991, *ApJ*, 377, 268  
 Gough, D. 1969, *JAtS*, 26, 448  
 Heger, A., Langer, N., & Woosley, S. 2000, *ApJ*, 528, 368  
 Kippenhahn, R., Weigert, A., & Weiss, A. 2012, Stellar Structure and Evolution (Berlin: Springer)  
 Kumar, P., Talon, S., & Zahn, J. 1999, *ApJ*, 520, 859  
 Lecoanet, D., & Quataert, E. 2013, *MNRAS*, 430, 2363  
 Moravveji, E., Aerts, C., Papics, P., Triana, S., & Vandoren, B. 2015, *A&A*, 580, A27  
 Moravveji, E., Townsend, R., Aerts, C., & Mathis, S. 2016, *ApJ*, 823, 130  
 Paxton, B., Bildstein, L., Dotter, A., et al. 2010, *ApJS*, 192, 3  
 Paxton, B., Marchant, P., Schwab, J., et al. 2015, *ApJS*, 220, 15  
 Pinsonneault, M. 1997, *ARA&A*, 35, 557  
 Press, W., & Rybicki, G. 1981, *ApJ*, 248, 751  
 Renzini, A. 1987, *A&A*, 188, 49  
 Rogers, T. 2015, *ApJL*, 815, L30  
 Rogers, T., & Glatzmaier, G. 2005, *MNRAS*, 364, 1135  
 Rogers, T., Lin, D., & Lau, H. 2012, *ApJL*, 758, 6  
 Rogers, T., Lin, D., McElwaine, J., & Lau, H. 2013, *ApJ*, 772, 21  
 Rogers, T., & MacGregor, K. 2010, *MNRAS*, 410, 946  
 Spruit, H. 2002, *A&A*, 381, 923  
 Sweet, P. 1950, *MNRAS*, 110, 548  
 Talon, S., & Charbonnel, C. 2005, *A&A*, 440, 981  
 Vogt, H. 1925, *AN*, 224, 245  
 Zahn, J. 1991, *A&A*, 252, 179